ORIGINAL RESEARCH ARTICLE

Kinetically Induced Fine Secondary α-Ti Phase Formation in a Novel As-Cast Titanium Alloy

ZHI LIANG, JIASHI MIAO, XUEJUN HUANG, FAN ZHANG, JIM C. WILLIAMS, and ALAN A. LUO

The formation of fine secondary hexagonal close packed (HCP) α-Ti precipitates provides major strengthening in a new Ti-6Al-5Fe-0.05B-0.05C (mass fractions in pct) cast alloy. The phase transformation mechanisms from the body-centered cubic (BCC) β-Ti matrix to fine α phase in this new α-β titanium alloy were investigated experimentally and computationally using CALculation of PHAse Diagram (CALPHAD)-based thermodynamic and kinetic models. The discrete distribution of α precipitates was observed in the as-cast alloy with evidence of strong Fe partitioning. Two main size groups of α precipitates and the Fe partitioning were characterized using scanning electron microscopy, scanning transmission electron microscopy, and synchrotron-based small-angle X-ray scattering techniques. A hypothesis of Fe-partitioning driven α precipitate nucleation and growth was validated by precipitation simulation using TC-PRISMA with customized thermodynamic and kinetic descriptions. These results suggested a new titanium alloy design route involving high-mobility elements (enhancing fine secondary α precipitates) and demonstrated the capability of CALPHAD-based modeling in titanium alloy design.

https://doi.org/10.1007/s11661-022-06775-2
© The Minerals, Metals & Materials Society and ASM International 2022

I. INTRODUCTION

HIGH strength, low density, and excellent corrosion resistance are the main properties that make titanium alloys attractive for a variety of applications, including aircraft, aero-engines, biomedical devices and chemical processing equipment.[1,2] However, high-volume application of titanium alloys in the automotive industry is hindered by the high costs of titanium and limited selection of available commercial Ti alloys. Ti–6Al–4V alloy, developed in 1954,[3] still dominates various wrought and cast products, although it was originally designed for wrought product applications at the time. Over the last few decades, the design of new titanium alloys has primarily used the conventional "trial-and-error" approach, which has been lengthy and costly. Recently, CALculation of PHAse Diagrams (CALPHAD) modeling, based on computational thermodynamics, has proved to be a valuable tool in alloy design under the ICME (Integrated Computational Materials Engineering) framework with successful examples in various alloy systems.[4] CALPHAD modeling can provide quick predictions of phase constituents and volume fractions for given alloy compositions, significantly increasing the alloy design space and efficiency, and reducing the extent of "trial-and-error" experimental work. CALPHAD modeling can also provide critical information for microstructure predictions, such as grain size,[5,6] alloying element segregation[7] and dissolution,[8] precipitation evolution[9] during solidification and thermomechanical processing. These new tools provide significant insights and guidance in alloy design and process development.

Recently, a new Ti–Al–Fe alloy was designed and developed using a CALPHAD-based approach.[10] The formation of the fine secondary α-Ti phase during cooling following solidification contributes to the excellent mechanical properties in this novel alloy. While the exact mechanisms for $\beta \rightarrow$ fine α transformation in Ti–Al–Fe alloys are unclear, it was speculated to be due to a combined effect from this specific system's thermodynamic driving force and kinetics.[10] There have been

ZHI LIANG is with the Department of Materials Science and Engineering, The Ohio State University, Columbus, OH 43210 and also now with the QuesTek LLC, 1820 Ridge Ave, Evanston IL 60201. JIASHI MIAO, XUEJUN HUANG, and JIM C. WILLIAMS are with the Department of Materials Science and Engineering, The Ohio State University. FAN ZHANG is with the Materials Measurement Science Division, Material Measurement Laboratory, National Institute of Standards and Technology, 100 Bureau Drive, Gaithersburg, MD 20899. ALAN A. LUO is with the Department of Materials Science and Engineering, The Ohio State University and also with the Department of Integrated Systems Engineering, The Ohio State University, Columbus, OH 43210. Contact e-mail: luo.445@osu.edu
Manuscript submitted April 3, 2022; accepted June 26, 2022.

Published online: 16 August 2022

several investigations on the $\beta \rightarrow$ fine α transformation mechanisms in commercial β titanium alloys such as Ti–5Al–5Mo–5V–3Cr (mass fraction in pct, Ti-5553).[11–15] Fine α homogenous precipitation in Ti-5553 was produced using a step-quenching method. The rapid temperature changes significantly increased the nucleation rate of the α phase but with a slight compositional variation.[11] Further investigation also found that a similar phenomenon could be triggered by fine precursory ω phase as nucleation sites for fine α.[12] In this novel Ti–Al–Fe alloy, the experimentally observed compositional difference between α and β phases from earlier work was significant and almost reached the equilibrium composition.[10] This observation suggests a new pathway for the formation of this fine secondary α, likely associated with strong elemental partitioning.

Since the formation of fine α precipitates is the major reason for higher strength in the new Ti–6Al–5Fe–0.05B–0.05C cast alloy, compared with cast commercial Ti–6Al–4V alloy, it is important to investigate the $\beta \rightarrow$ fine α transformation. In this paper, CALPHAD modeling and key characterizations, including scanning electron microscopy (SEM), transmission electron microscopy (TEM), and small angle X-ray scattering (SAXS) measurements, were set out to reveal the exact mechanisms of this kinetically induced fine secondary α-Ti phase formation. SEM/TEM and SAXS measurements provided morphological observation and quantitative measurements of the fine secondary α-Ti respectively, and both characterizations were consistent with the CALPHAD phase transformation modeling results. This investigation reveals a critical phase transformation pathway for titanium alloy design, enabling future titanium alloy development.

II. $\beta \rightarrow \alpha$ TRANSFORMATION MECHANISM HYPOTHESIS

Iron (Fe) is one of the strongest β stabilizers in Ti alloys. However, Fe is notorious for causing "β fleck" (β-stabilizer-rich defects) in ingot metallurgy products, due to its fast diffusion and thus solute segregation during freezing of the last Fe-rich liquid. Therefore, traditional Ti alloys always limit or exclude Fe content to avoid this problem. But in recent years, the emergence of processes with high cooling rates such as permanent mold casting and additive manufacturing skips the slower cooling rate ingot metallurgy step. Therefore, the involvement of high-kinetics elements, such as Fe, can be considered again. Our earlier work reported an interesting as-cast microstructure of a novel Ti–Al–Fe alloy, which contained a fine secondary α phase, contributing to its excellent mechanical properties.[10] Since the secondary α phase is generally produced by heat treatment in titanium alloys, its formation in the as-cast condition is surprising and different from the other $\beta \rightarrow$ fine α formation mechanisms reported.[11–15]

As shown in the as-cast microstructure of a new Ti–Al–Fe alloy in Figure 1, the $\beta \rightarrow \alpha$ nucleation and growth process lead to two populations of α precipitates with distinct sizes. Generally, as-cast α-β titanium alloys show either lamellar or basket-weave microstructure depending on their cooling conditions, but the α phase size distribution is mostly continuous.[16] As schematically depicted in Figure 2, during the formation of a lamellar structure, the primary α nucleates initially at the β grain boundary. These primary α precipitates serve as the heterogeneous nucleation sites for the secondary α at the α/β-phase matrix interfaces. The lamellar growth dominates the subsequent phase transformation. In contrast, the basket-weave alpha microstructure forms during higher cooling rates where the transformation is nucleation rate dominated. In this case, tertiary α heterogeneously nucleates on the boundary between lamellar α and the remaining β matrix. The growth of α phase obeys the Burgers orientation relationship, thus forming the basket-weave microstructure. This magnitude of slow cooling rates is usually achieved in post-casting heat treatment rather than the direct cooling during casting.

In this work, due to the addition of a grain refiner (boron) which promotes the formation of TiB at the β grain boundary, the grain boundary α phase is not continuous.[10,16] Our experimental observations suggest that after the nucleation and growth of the primary α, the secondary α homogenously nucleates from the remaining β matrix. The is likely due to strong Fe partitioning from the primary α to the β matrix, leading to a Fe-enriched remaining β matrix. At the beginning, the Fe-enriched β matrix has high nucleation barrier for secondary α formation, but as the cooling continues, this nucleation barrier will decrease, and the nucleation will resume. In the experiment, a characteristic discontinuous size difference between primary and secondary α is shown in Figure 3, indicating that this secondary nucleation has a much higher nucleation rate than the primary one. With a high nucleation density, the independent growth of these secondary α precipitates becomes limited and results in the fine secondary α phase, as illustrated in Figure 4. This hypothesis is based on two assumptions: (1) the Fe partitioning between primary α and β matrix is fast enough under high cooling rates; and (2) the super-saturated β matrix after Fe partitioning can introduce both high driving force and nucleation rate for secondary α precipitate formation as the schematics shown in Figure 5. As cooling proceeds, due to the fast diffusion of Fe in β matrix, ($\beta \rightarrow \alpha + \beta$) diffusional transformation will rapidly occur, which leads to the over-saturation of the newly formed β phase. Though the driving force might not be sufficient for the transformation to occur immediately, as further cooling proceeds, this driving force will increase and trigger the diffusion transformation. This hypothesis was investigated with precipitation simulations using established thermodynamic and kinetic databases and experimental measurements.

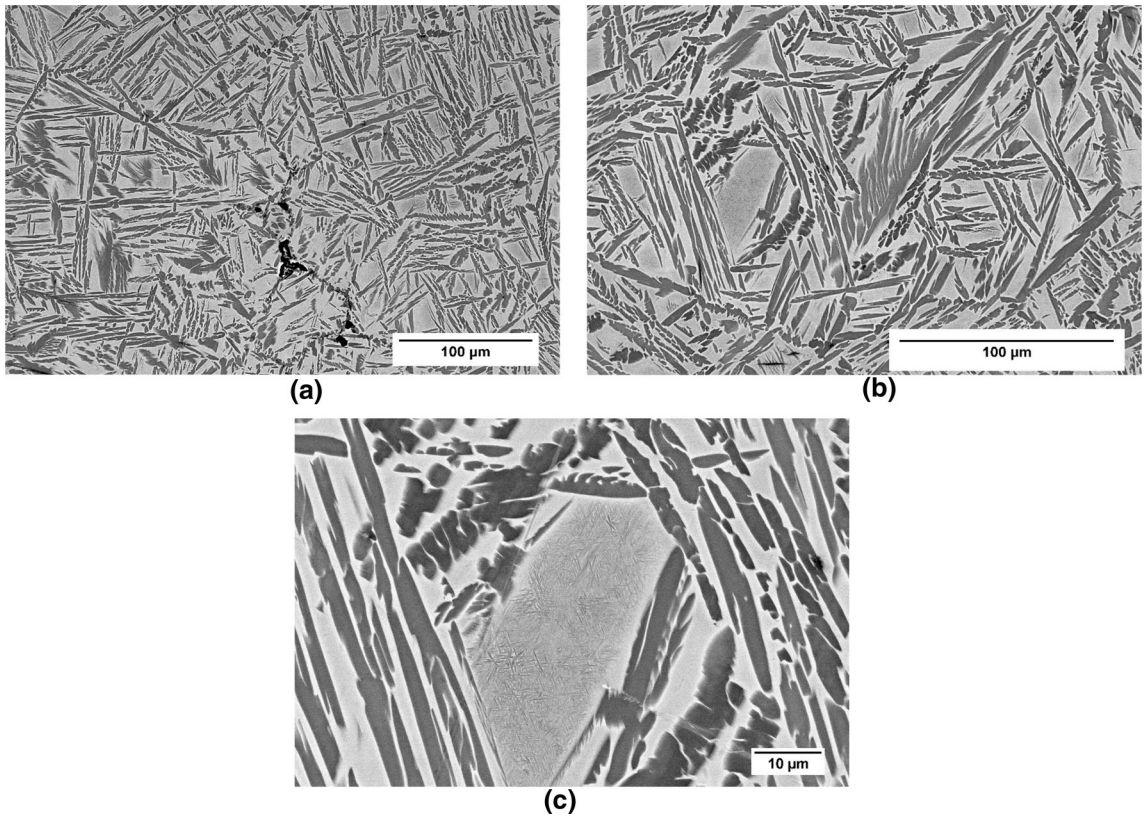

Fig. 1—SEM images of as-cast Ti-6Al-5Fe-0.05B-0.05C alloy (mass fraction in pct) microstructures at different magnifications (*a*) through (*c*), in which (c) shows a clear cluster of secondary α phase surrounded by significant different size of primary α phase.

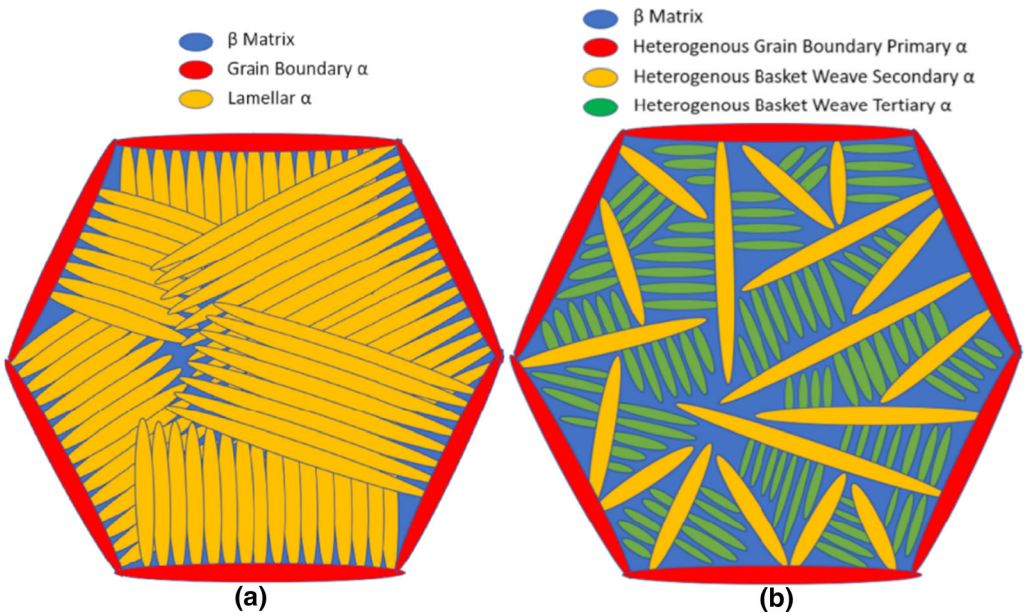

Fig. 2—(*a*) Lamellar (the overlap between lamellar α does not indicate actual overlap but only drawing purpose) and (*b*) basket-weave microstructures schematics.

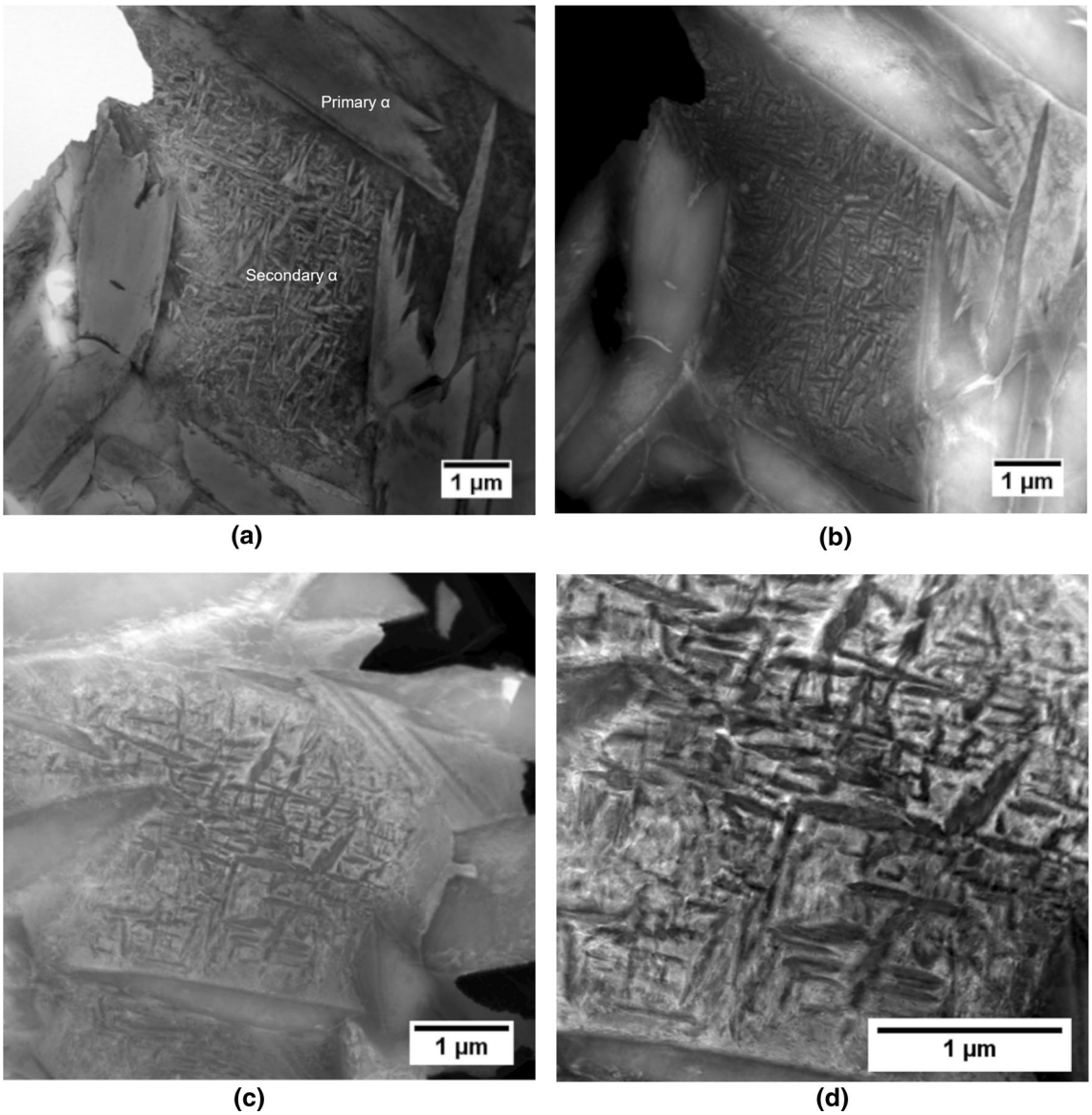

Fig. 3—STEM characterization of the secondary α in as-cast Ti-6Al-5Fe-0.05B-0.05C: (*a*) Bright field STEM and (*b*) HAADF-STEM images showing the significant difference in size between primary and secondary α, (*c*) and (*d*) HAADF-STEM images of zoom-in secondary α.

III. EXPERIMENTAL PROCEDURES

A. *Sample Preparation and Microstructure Characterization*

An experimental alloy with a nominal composition Ti–6Al–5Fe–0.05B–0.05C (all mass fraction in pct, boron and carbon are added for β grain refinement) reported in an earlier publication[10] was prepared by induction skull melting. Scanning electron microscopy (SEM) and transmission electron microscopy (TEM) were used for microstructure, morphology, and compositional analysis. SEM characterization was conducted using a FEI Apreo* microscope, operated at 20 kV.

*Certain commercial equipment, instruments, software or materials are identified in this paper to foster understanding. Such identification does not imply recommendation or endorsement by the Department of Commerce or the National Institute of Standards and Technology, nor does it imply that the materials or equipment identified are necessarily the best available for the purpose.

Blanks for TEM foils were sectioned from as-cast specimens using a low-speed diamond saw. The foils were mechanically ground to a thickness of about 100 μm. Final thinning and perforation of the TEM foils were completed by electro-polishing in an electrolyte containing 5 pct perchloric acid, 35 pct butyl cellosolve and 55 pct methanol at a temperature of – 30 °C and an applied voltage of 30 V. TEM characterization was performed on an image-corrected and mono-chromated Titan3 60-300 microscope equipped with a SuperX EDS system and operated at 300 keV.[10]

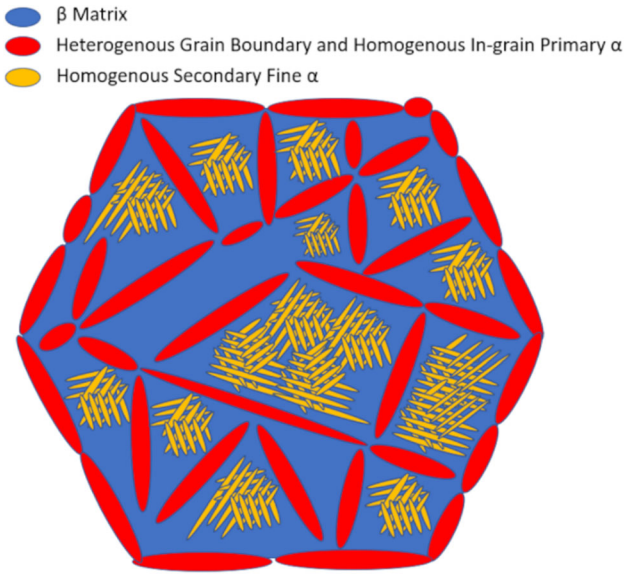

Fig. 4—Homogeneous nucleation of primary and secondary α formation schematic (the overlap between secondary α does not indicate actual overlap but only drawing purpose).

As reported previously, the as-cast microstructure of the new Ti–Al–Fe alloy contained morphologically similar α phase but with very different precipitate sizes as shown in Figure 3. Upon close examination of Figures 3(b) and (c), it can be seen that although the morphology was similar to basket-weave type, the secondary α phase was different from the commonly observed basket-weave morphology in α-β titanium alloys (in Ti–6Al–4V alloy, for example Reference 17). The first primary α phase formed (the largest size α phase in microstructure which presumably nucleated and grew first) did not adhere to the secondary ones, which was indicated by the precipitation free zone between primary and secondary α phases. This observation showed that the secondary α phase did not nucleate heterogeneously on the primary α, and instead, nucleated in the remaining β matrix (after primary α formation). Though the Fe-enriched β matrix will reduce the driving force for secondary α formation, but as the cooling continues, the driving force will increase and resume the nucleation, which, depending on the observation of larger amount of secondary α, indicates a much larger driving force in this stage. It is noted that the fine α phase only exists in the space between primary α precipitates. These regions are large enough that diffusion lengths required for lateral contraction is not possible, and thus the precipitation of

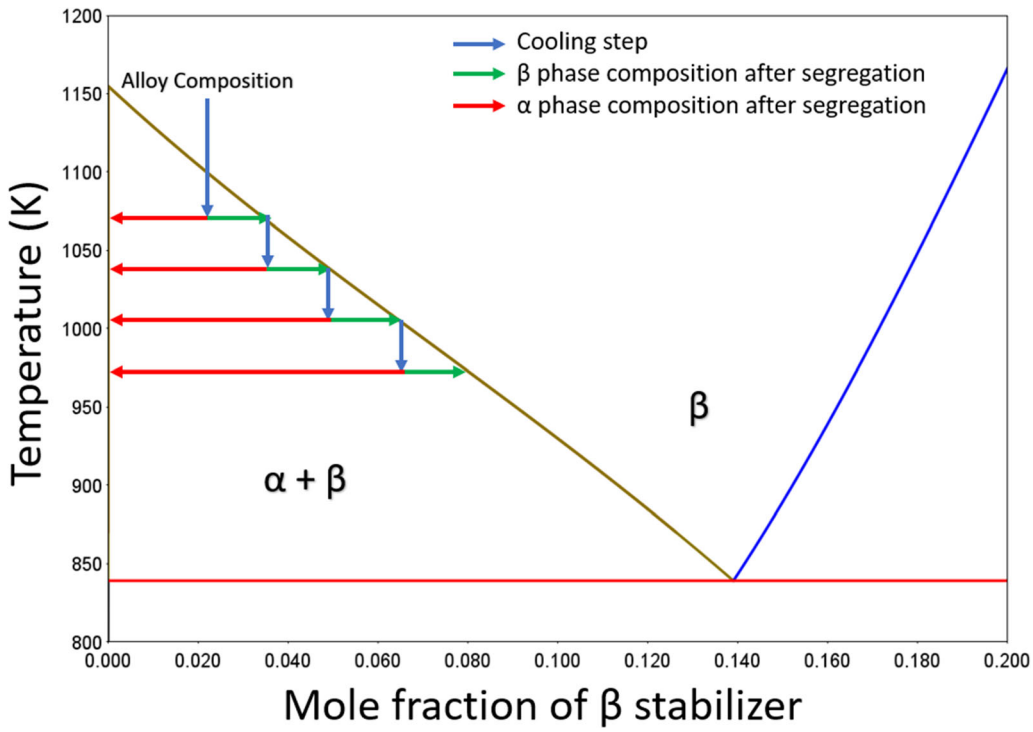

Fig. 5—Schematic phase diagram of α and β phases compositions evolution during cooling with fast kinetics β stabilizer (the number of steps illustrated in the schematics do not refer to the real number of cooling steps).

secondary α phase is allowed. Also, according to the STEM-EDS result in earlier work,[10] the primary α phase showed a strong Fe depletion into the β matrix, suggesting that the kinetics of Fe in this alloy was likely the main cause of the nucleation event increase and dominated the phase transformation mechanism. This observed partitioning also corroborates the schematic in Figure 5, suggesting that with high Fe concentration at the α/β interface, such local α nucleation is not preferred due to insufficient driving force.

B. *Small angle X-ray scattering (SAXS) measurement*

Small-angle X-ray scattering measurements were performed on the Ti–Al–Fe alloy specimen in transmission geometry at sector 9-ID of the Advanced Photon Source (APS) of Argonne National Laboratory. The sample thickness was 0.35 mm. This instrument combines a Bonse-Hart type ultra-small angle X-ray scattering setup with a high-sensitivity pinhole SAXS setup. It provides absolute scattering intensity over a q range from $\approx 1 \times 10^{-4}$ Å^{-1} to ≈ 1 Å^{-1}. Here $q = 4\pi/\lambda \sin(\theta)$, where λ is the monochromatic wavelength ($\lambda = 0.5904$ Å, corresponding to X-ray energy of 21 keV) used for this measurement and θ is one half of the scattering angle 2θ. A high photon density (1×10^{13} photon/(s mm^2)), large sample volume (beam size 0.8 mm × 0.8 mm), and a high X-ray detection efficiency ensure the capture of statistically meaningful microstructural information. More details about this instrument can be found elsewhere.[18]

IV. FINITE ELEMENT MODELLING OF AS-CAST COOLING PROFILE

To acquire the cooling curve of the as-cast sample, finite element modelling was carried out using casting simulation software, ProCAST, as thermal couple was not possible in the vacuum induction furnace in this work. The molten titanium alloy was solidified in a water-cooled copper crucible with inner diameter of 60 mm and wall thickness of 10 mm. In the simulation, the initial temperature of the molten titanium alloy was 2000 °C, and the initial temperature of the crucible was 200 °C. The outside of the copper crucible was set at 20 °C, because there was chill water constantly circulating around the crucible. The thermal conductivity of the alloy was calculated from CALPHAD predictions. Figure 6 shows the thermal conductivity as a function of temperature. Specific heat and latent heat of this alloy are set as constant at 1100 J/(kg K) and 288 kJ/kg (Ti-64 data in ProCAST database). The heat transfer coefficient between the alloy and the crucible is calibrated as constants with 1000 W/(m^2 K) above liquidus temperature and 100 W/(m^2 K) below solidus temperature. The heat transfer coefficient changes linearly between the liquidus and solidus temperature.[19] The simulated cooling profile is used as the input for the precipitation simulation.

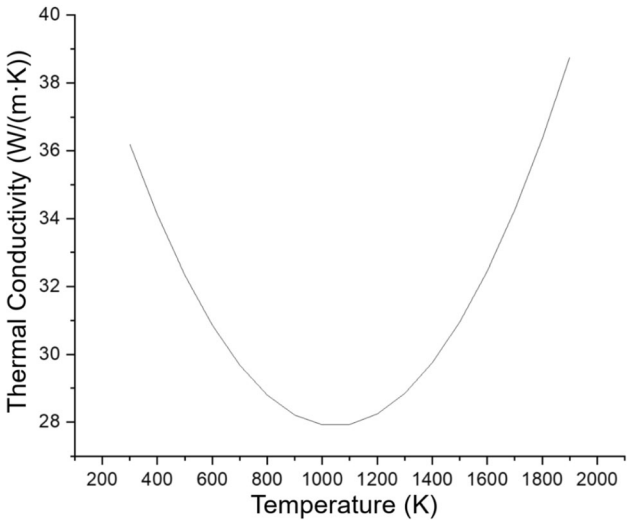

Fig. 6—Thermal conductivity of Ti–Al–Fe as a function of temperature, which is based on CALPHAD simulation.

V. CALPHAD MODELING

A. *Thermodynamic and Kinetic Descriptions of Ti–Al–Fe System*

As illustrated in Section III, thermodynamic and kinetic descriptions of participating phases are necessary in phase transformation modeling, providing basis for alloy equilibrium conditions, thermodynamic driving force, atomic mobility, etc. Since there are no comprehensive commercial databases for Ti–Al–Fe ternary system, customized Ti–Al–Fe thermodynamic and kinetic descriptions were established in prior work[20] and applied in this investigation. Boron and carbon are not major alloying elements but act as grain refiners, and therefore are not included in this description to simplify the modeling. A comprehensive database for the entire composition regime is still under development, but the α and β phase descriptions in Ti-rich corner are sufficient for this work. As shown in Figures 7 and 8, the equilibrium pathway of Ti–6Al–5Fe represents the reasonable β transus, and the partitioning of Al and Fe in α and β phases also represents clear difference, correlating with the composition measurements in earlier work.[10] As for kinetic database, since only

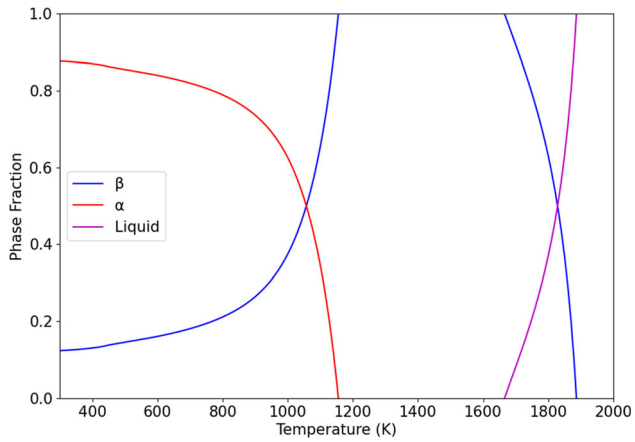

Fig. 7—Equilibrium pathway of Ti–6Al–5Fe.

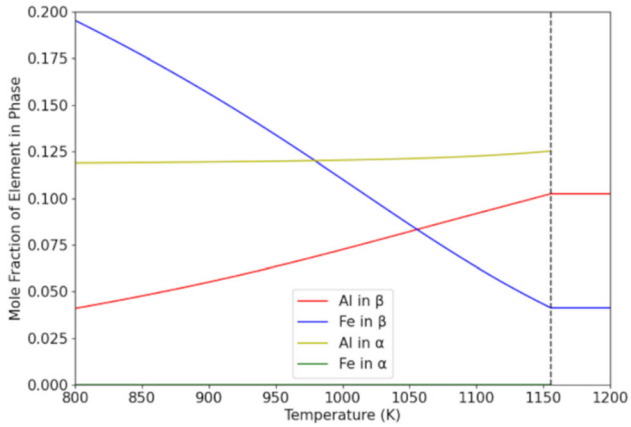

Fig. 8—Elemental segregation during equilibrium pathway of Ti–6Al–5Fe. Fe in α is nearly 0, and is plotted at the bottom of the figure.

tracer and impurity diffusivities were involved,[21–26] its limitation was recognized.

B. *Nucleation and Growth Rate Model*

In this work, Kampmann–Wagner numerical (KWN) model[26] is applied using the TC-PRISMA module in ThermoCalc software.[27] Within the KWN framework, the classical nucleation and general (Morral–Purdy) growth rate models are chosen.

1. *Nucleation*

The time-dependent nucleation rate is expressed by Eq. [1][28]:

$$J^* = \beta^* Z N \exp\left(-\frac{\Delta G^*}{kT}\right)\exp\left(-\frac{\tau}{t}\right), \quad [1]$$

where N is the nucleation site density; k is Boltzmann's constant; T is temperature; t is time. ΔG^* is the critical nucleus formation energy and defined as[27]:

$$\Delta G^* = \frac{16\pi\gamma^3}{3(\Delta G^{\beta\to\alpha}/V_{\mathrm{m}}^{\alpha})^2} \quad [2]$$

where γ is the interfacial energy, which is calculated with coherent bond counting model, directly using calculated bulk Gibbs-free energy of α and β phases[27]; $\Delta G^{\beta\to\alpha}$ is the phase transformation driving force; V_{m}^{α} is the molar volume of the precipitate phase. β^* is the rate of atomic transfer at the nucleus–matrix boundary and defined as[27]:

$$\beta^* = \frac{4\pi r^{*2}}{a^4}\left[\sum_{i=1}^{k}\frac{(x_i^{\alpha/\beta} - x_i^{\beta/\alpha})^2}{x_i^{\beta/\alpha} D_i}\right]^{-1}, \quad [3]$$

where $x_i^{\alpha/\beta}$ and $x_i^{\beta/\alpha}$ are elemental compositions at the interface at precipitate (α) and matrix (β) sides (precipitate/matrix); a is the atomic jump distance at interface, equal to lattice parameter; D_i is the matrix diffusion coefficient; r^* is the critical nucleus radius and defined as[27]:

$$r^* = -\frac{2\gamma V_{\mathrm{m}}^{\alpha}}{\Delta G^{\beta\to\alpha}}, \quad [4]$$

Z is the Zeldovich non-equilibrium factor and defined as[27]:

$$Z = \frac{V_m^{\alpha}}{2\pi N_{\mathrm{A}} r^{*2}}\sqrt{\frac{\gamma}{kt}} \quad [5]$$

τ is the incubation time and defined as[29]:

$$\tau = \frac{1}{2Z^2\beta^*} \quad [6]$$

It should be noted that in nucleation model, the initial nucleus size is small and can be approximated as spherical regardless of its geometry, which is considered in the growth model.

As shown in Figure 1, neither the primary nor secondary α phase is specifically located on grain boundaries, but more evenly distributed as illustrated in the schematic in Figure 4. Furthermore, the gaps between primary and secondary α also indicate that the secondary α does not nucleate on the primary α boundaries. Therefore, the nucleation site type is defined as bulk homogenous nucleation. However, it is well-known that homogenous nucleation has relatively high energy barrier. It is more likely that at least part of α phase is nucleated from in-grain dislocations. But since the determination of dislocation density is complex, in this work, bulk homogenous nucleation site is applied.[27,30] Also, as observed from the microstructure in Figure 3, morphologies of both α phases are needle-like and thus are modelled as the ellipsoidal needle-geometry, with an aspect ratio ($\frac{l}{a}$) of 3 for the precipitate nuclei, in which l and a are the length and width of the precipitate respectively.

2. *Growth*

The simplified growth rate model is a quasi-steady state approximation.[24] The growth rate is expressed by[27]:

$$v = \frac{2\gamma V_m^{\alpha} K}{r}\left(\frac{1}{r^*} - \frac{1}{r}\right), \quad [7]$$

where r is the current precipitate size; K is the kinetic parameter defined as[27]:

$$K = \left[\sum \frac{(x^{\beta/\alpha}(r) - x^{\alpha/\beta}(r))^2 \xi_i}{x^{\beta/\alpha}(r) M_i}\right]^{-1}, \quad [8]$$

where $x^{\beta/\alpha}(r)$ and $x^{\alpha/\beta}(r)$ are the elemental compositions of precipitate and matrix phases at precipitate-matrix interface; and M_i is the corresponding atomic mobility in the matrix; and ξ_i is the effective diffusion distance factor for each independent component i, represented by $\xi_i = \frac{\Omega_i}{2\lambda_i^2}$, where $\Omega_i = \frac{x_i^{\beta} - x_i^{\beta/\alpha}}{x_i^{\alpha/\beta} - x_i^{\beta/\alpha}}$ as dimensionless supersaturation for different component, and $2\lambda_i^2 - 2\lambda_i^3\sqrt{\pi}\exp(\lambda_{\mathrm{i}}^2)\mathrm{erfc}(\lambda_{\mathrm{i}}) = \Omega_i$.

3. *Mobility description*

The mobility description is based on the binary impurity and self-diffusion data of Ti, Al and Fe in the BCC β-phase matrix. Kinetic calculations in ternary regime are generally based on extrapolation of binary data. In this simulation, a mobility enhancement prefactor (MEP) was modified as reflection of mobility data, which is a temperature-independent multiplier factor for diffusion frequency factor, D_0. MEP in this work is defined as 100. Since there are discrepancies of D_0 among different mobility assessments, a multiplier within two orders of magnitude of difference is acceptable.[31] This modification indicates potential effect from undefined binary and ternary interaction parameters in the kinetic description.

4. *Molar volumes of matrix (β) and precipitate (α) phases*

Molar volumes of disordered BCC and HCP phases are modeled in the database with simple rule of mixture as Eq. 9:

$$V_m = \sum_i x_i {}^m V_i, \qquad [9]$$

where x_i is the mole fraction of the element, and ${}^m V_i$ is the molar volume of pure element in phase m. The molar volumes of BCC/HCP Ti and BCC Fe are acquired from experiments,[32] while the molar volumes of HCP Fe and BCC/HCP Al are acquired from first-principle calculation since they are metastable.[33,34] For simplicity, all pure element molar volumes are considered temperature-independent and only composition-dependent. The molar volume contour maps of BCC and HCP phases are shown in Figure 9. Though Lu *et al.*[35] assessed the temperature-dependence of experimental molar volume for pure elements, applying the temperature-dependence may cause conflicts with first-principle calculated metastable phase parameters. Therefore, the temperature-dependence is ignored in this work.

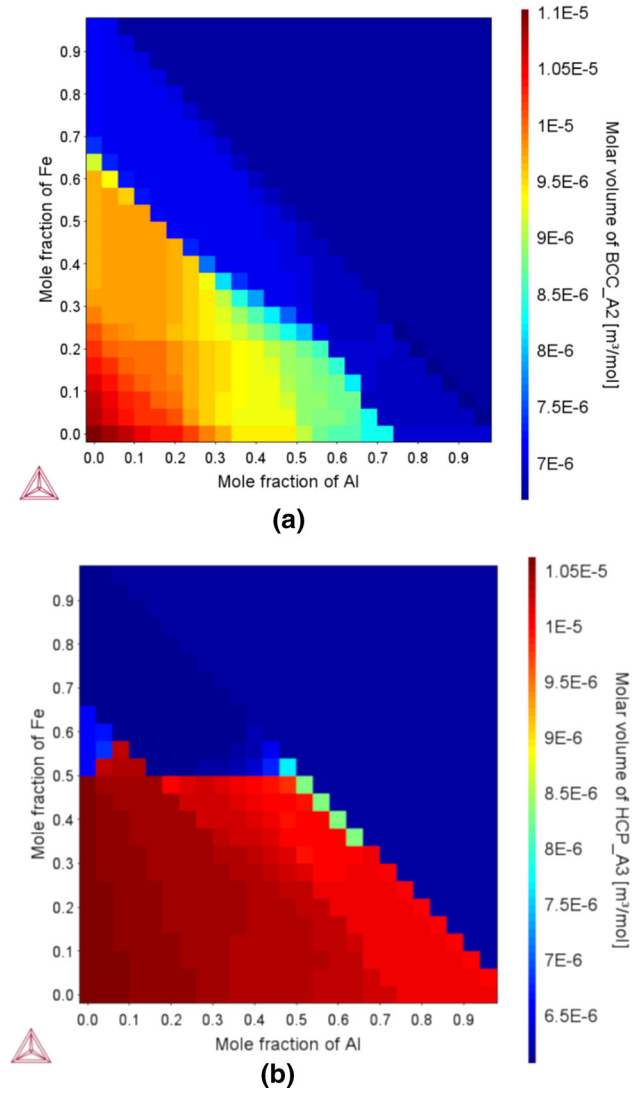

Fig. 9—Composition-dependent molar volume maps of (*a*) β (BCC_A2) and (*b*) α (HCP_A3) phases.

VI. RESULTS AND DISCUSSION

A. *Cooling Analysis During Casting*

The FEM simulated cooling profile at the center of the as-cast specimen is shown in Figure 10. It can be seen that, except for the initial fast cooling in 50 seconds, the rest of the cooling profile is close to parabolic, which has gradually decreased cooling rate. The cooling profile is used as the input for precipitation simulation.

B. *α Nucleation Rate and Driving Force Evolution*

Figure 11 shows the calculated evolution of α nucleation rate and its driving force with temperature profile. As cooling proceeds, both nucleation rate and driving force indicate two separate α nucleation events at approximately 880 °C and 625 °C, respectively. There is clearly a gap in the nucleation rate curve, where the nucleation rate drops to less than 10^{-30} nuclei/(m^3 s^1) (less than 10^{-57} nuclei/(nm^3 s^1)). The first nucleation rate

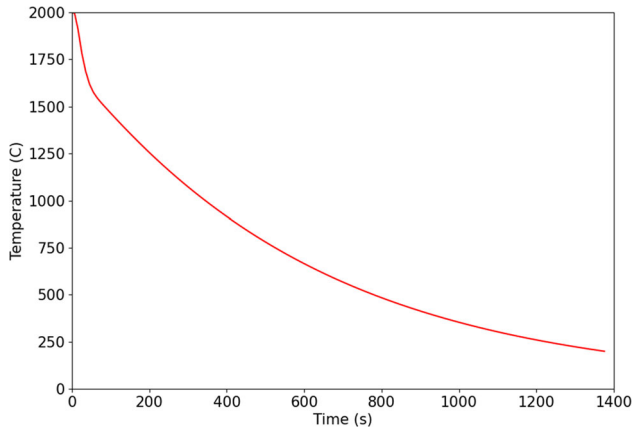

Fig. 10—ProCAST simulated cooling profile at the center of the as-cast specimen.

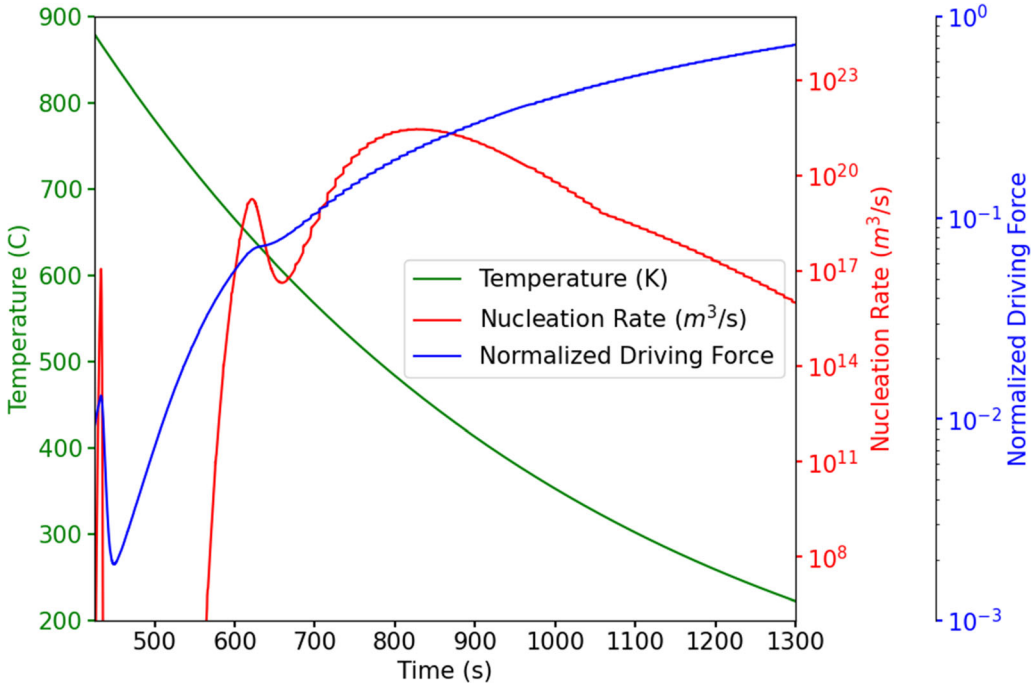

Fig. 11—Calculated evolution of α nucleation rate, driving force, and temperature profile.

peak and the subsequent gap represent the primary α formation and its growth happening in a short time period, resulting in smaller number density but larger size of α precipitates. The second nucleation rate peak represents the secondary α formation happening in an extended time period, which results in higher number density but smaller size of α precipitates. This simulation output correlates well with the experimental observation of the discontinuous α size distribution.

C. *Comparison with Experimental Results*

The synchrotron SAXS data were analyzed to provide a bulk and statistically meaningful description of the size distribution of the α phase. It was assumed that a two-phase system, *i.e.*, α precipitates embedded in the β matrix in the analysis, and the precipitates have an ellipsoidal shape with a length to diameter ratio of 3, consistent with the SEM observation and the model assumption. A maximum-entropy small-angle scattering analysis approach was used,[36] to avoid any possible bias introduced by assumed size distribution. Figure 12 shows the comparison between the α-phase volume densities measured by SAXS and predicted by PRISMA simulations. Overall, the simulation and the experimental result show remarkable agreement. The size distribution shows two separated segments and a notable gap at approximately 1 μm, with the smaller segment being secondary α and the larger one being primary α. The size distribution of the secondary α is broad, with a maximum near 700 Å in both experiments and simulations, while that of the primary α is considerably narrower, with a maximum at approximately 3 μm. It should be pointed out that the SAXS results are not direct measurements of the precipitates. To properly evaluate the absolute volume fractions of the primary and secondary α, more information, such as the local mass density and electron density variation near the precipitates, is required. Nevertheless, the data demonstrate that the PRISMA simulation captured the essence of the precipitation of the α phases in a bulk volume of the new Ti–Al–Fe alloy.

As described in Section V–B–1, the nucleation in this work was assumed to be homogenous. Therefore, the initial available nucleation sites in the simulation were calculated based on the matrix phase and each atom in the matrix phase was a potential nucleation site.[26] However, different from the case of Ti-5553,[12] the experimental alloy in this investigation was directly cooled from the liquid state without any annealing step to eliminate heterogenous nucleation sites such as vacancies and dislocations. Thus, it was reasonable to assume that at least some precipitates could heterogeneously nucleate on dislocations (the possibility of heterogenous nucleation on primary α boundaries were excluded based on experimental observation). However, the secondary α morphology conflicted with the assumption of complete dislocation-based heterogenous nucleation. Because based on experimental observation, under such assumption, the nucleation site density for the secondary α was significantly higher than primary α, and further implied a non-uniform spatial distribution of the dislocation density across the microstructure.

It is reasonable to surmise that the actual nucleation should have a combination of both heterogenous and homogenous mechanisms: heterogenous for primary α

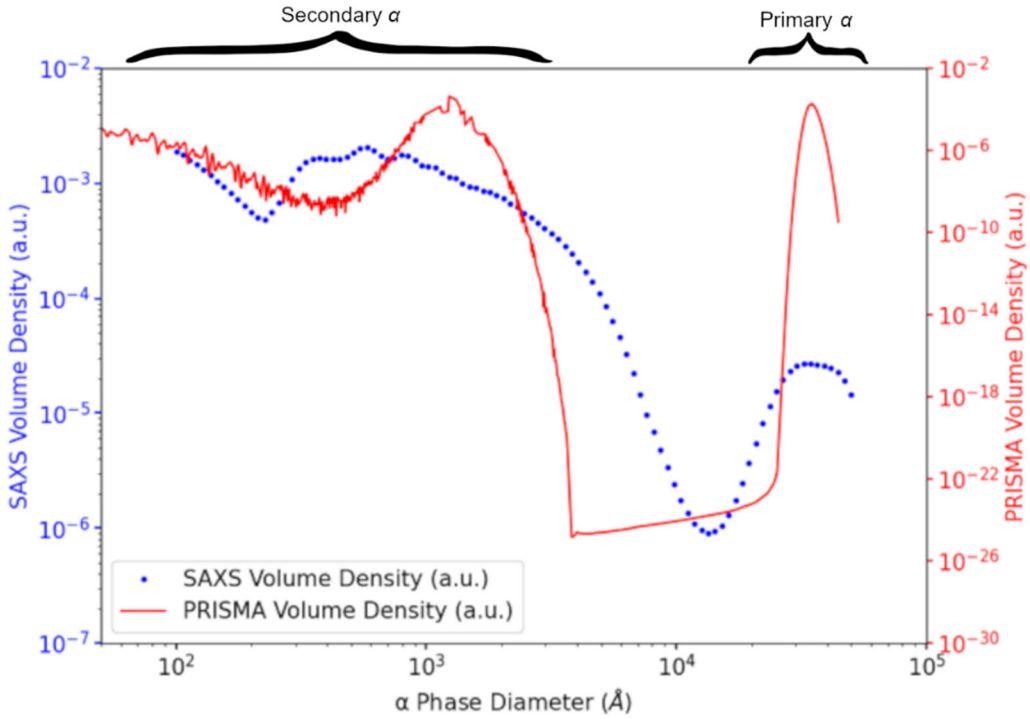

Fig. 12—Comparison between PRISMA simulation and SAXS measurement results.

and homogenous for secondary α. However, it is not possible to create such boundary conditions in the present TC-PRIMSA model, and it is difficult to estimate the dislocation density for primary α phase only. The number density of α precipitates might not quantitatively reflect the experimental results, but the size discontinuity was still proved. The other limitation of the current model is the simplification of mobility description, resulting in the usage of MEP. However, as discussed in Section V–B–3, this modification factor is not considered to be significant, and is expected to be resolved with fully assessed mobility description.

The actual cooling profile in casting processes could be different from the FEM simulation. The cooling rate would likely affect the magnitude of Fe partitioning out of primary α regime to the remaining β regime. However, since Fe has almost zero solubility in α-Ti, its partitioning could be more contributed by thermodynamic stability than kinetic transport, meaning that Fe partitioning would not be significantly affected by the cooling rate. Nonetheless, cooling rate would affect (1) the homogenization of Fe in remaining β, and (2) growth of primary and secondary α. Thus, the following two scenarios can be hypothesized based on potential different cooling profiles: (1) with higher overall cooling rate, primary α will be smaller while secondary α remains similar size but larger fraction, and (2) with lower cooling rate, the primary α will be larger while secondary α remains similar size but a smaller fraction. Additionally, precipitate-free zones (PFZs) between primary and secondary α will be smaller at higher cooling rates, which in this simulation will be reflected on the size distribution peaks in Figure 12.

VII. CONCLUSIONS

In this work, the formation mechanisms of primary and secondary α precipitates in Ti–Al–Fe system, specifically for a new high-strength alloy Ti–6Al–5Fe–0.05B–0.05C, are investigated using a CALPHAD-based phase transformation model and validated by TEM and SAXS experimental results, with the following conclusions:

1. The $\beta \rightarrow \alpha$ phase transformation in Ti–Al–Fe alloy system is modeled with our new thermodynamic and kinetic descriptions and the simulation agrees well with the experimental results.
2. In Ti–Al–Fe system, the elemental segregation, mainly Fe, introduces a significant increase in nucleation driving force, and therefore leads to a higher secondary nucleation peak during solid state $\beta \rightarrow (\alpha + \beta)$ phase transformation. With higher nucleation rate in a smaller spatial regime, the secondary nuclei only have limited growth and resulted in a very fine secondary α phase.
3. The fast partitioning of Fe leads to "*in-situ equilibrium*", in which the β matrix continues to reach equilibrium composition during phase transformation. This is mainly due to the high mobility of β stabilizer, and also contributes to the nucleation driving force and growth rate as explained in Section II with Figure 5 *via* facilitating ultra-fine secondary α formation at lower temperature.
4. The formation of fine secondary α phase *via* elemental partitioning, without complex thermo-mechanical treatment procedures, offers an important avenue to achieve high strength in as-cast

titanium alloys. Upon selection of alloying elements, the criterion of high mobility and driving force changes during phase transformation provide critical new vision in titanium alloy design and development.

ACKNOWLEDGMENTS

We thank Drs. Carelyn E. Campbell, Ursula Kattner, and Kil-Won Moon at National Institute of Standards and Technology for helpful discussions on thermodynamic and kinetics descriptions used in this work. Use of the Advanced Photon Source, an Office of Science User Facility operated for the U.S. Department of Energy (DOE) Office of Science by Argonne National Laboratory, was supported by the U.S. DOE under Contract No. DE-AC02-06CH11357. This investigation is sponsored by the U.S. Department of Energy under project DE-EE0006858. This report was prepared as an account of work sponsored by an agency of the United States Government. Neither the United States Government nor any agency thereof, nor any of their employees, makes any warranty, express or implied, or assumes any legal liability or responsibility for the accuracy, completeness, or usefulness of any information, apparatus, product, or process disclosed, or represents that its use would not infringe privately owned rights. Reference herein to any specific commercial product, process, or service by trade name, trademark, manufacturer, or otherwise does not necessarily constitute or imply its endorsement, recommendation, or favoring by the United States Government or any agency thereof. The views and opinions of authors expressed herein do not necessarily state or reflect those of the United States Government or any agency thereof.

CONFLICT OF INTEREST

On behalf of all authors, the corresponding author states that there is no conflict of interest.

REFERENCES

1. G. Lütjering and J.C. Williams: *Titanium*, 2nd ed. Springer, Berlin, 2007.
2. D. Banerjee and J.C. Williams: *Acta Mater.*, 2013, vol. 61(3), pp. 844–79.
3. F.H. Froes: *Titanium: Physical Metallurgy, Processing, and Applications*, ASM International, Materials Park, OH, 2015.
4. A.A. Luo: *CALPHAD*, 2015, vol. 50, pp. 6–22.
5. C. Gu, Y. Lu, E. Cinkilic, J. Miao, A. Klarner, X. Yan, and A.A. Luo: *Comput. Mater. Sci.*, 2019, vol. 161, pp. 64–75.
6. C.D. Ridgeway, C. Gu, and A.A. Luo: *J. Mater. Sci.*, 2019, vol. 54, pp. 9907–920.
7. C. Zhang, J. Miao, S. Chen, F. Zhang, and A.A. Luo: *J. Phase Equilib. Diffus.*, 2019, vol. 40, pp. 495–507.
8. R. Shi, J. Miao, and A.A. Luo: *Scripta Mater.*, 2019, vol. 171, pp. 92–7.
9. X. Xia, W. Sun, A.A. Luo, and D.S. Stone: *Acta Mater.*, 2016, vol. 111, pp. 335–47.
10. Z. Liang, J. Miao, T. Brown, A.K. Sachdev, J.C. Williams, and A.A. Luo: *Scripta Mater.*, 2018, vol. 157, pp. 124–28.
11. S. Nag, Y. Zheng, R.E.A. Williams, A. Devaraj, A. Boyne, Y. Wang, P.C. Collins, G.B. Viswanathan, J.S. Tiley, B.C. Muddle, R. Banerjee, and H.L. Fraser: *Acta Mater.*, 2012, vol. 60, pp. 6247–256.
12. Y. Zheng, R.E.A. Williams, J.M. Sosa, T. Alam, Y. Wang, R. Banerjee, and H.L. Fraser: *Acta Mater.*, 2016, vol. 103, pp. 165–73.
13. Y. Zheng, R.E.A. Williams, J.M. Sosa, Y. Wang, R. Banerjee, and H.L. Fraser: *Scripta Mater.*, 2016, vol. 111, pp. 81–4.
14. Y. Zheng, R.E.A. Williams, D. Wang, R. Shi, S. Nag, P. Kami, J.M. Sosa, R. Banerjee, Y. Wang, and H.L. Fraser: *Acta Mater.*, 2016, vol. 103, pp. 850–58.
15. A. Boyne, D. Wang, R.P. Shi, Y. Zheng, A. Behera, S. Nag, J.S. Tiley, H.L. Fraser, R. Banerjee, and Y. Wang: *Acta Mater.*, 2014, vol. 64, pp. 188–97.
16. S. Roy, S. Suwas, S. Tamirisakandala, D.B. Miracle, and R. Srinivasan: *Acta Mater.*, 2011, vol. 59, pp. 5494–510.
17. D.M. Stefanescu and R. Ruxanda: in: G.F. Vander Voort, ed., *Metallography and Microstructures*, ASM International, Materials Park, OH, 2004.
18. J. Ilavsky, F. Zhang, R.N. Andrews, I. Kuzmenko, P.R. Jemian, L.E. Levine, and A.J. Allen: *J. Appl. Crystallogr.*, 2018, vol. 51, pp. 867–82.
19. P.A. Kobryn and S.L. Semiatin: *Metall. Mater. Trans. B*, 2001, vol. 32B, pp. 685–95.
20. Z. Liang, I. Zhirnov, F. Zhang, K.K. Jones, D. Deisenroth, M. Williams, U. Kattner, K. Moon, W. Liu, B. Lanes, and C.E. Campbell: *Materialia*, 2020, vol. 14, 100934.
21. J.F. Murdock, T.S. Lundy, and E.E. Stansbury: *Acta Metall.*, 1964, vol. 12, pp. 1033–039.
22. R.J. Borg and C.E. Birchenall: *Trans. Met. Soc. AIME*, 1960, vol. 218, pp. 980–84.
23. I.A. Akimova, V.M. Mironov, and A.V. Pokoyev: *Fiz. Met. Metall.*, 1983, vol. 56, pp. 1225–227.
24. H. Araki, T. Yamane, Y. Minamino, S. Saji, Y. Hana, and S.B. Jung: *Metall. Mater. Trans. A*, 1994, vol. 25A, pp. 874–76.
25. H. Wu, T. Mayeshiba, and D. Morgan: *Sci. Data*, 2016, https://doi.org/10.1038/sdata.2016.54.
26. G.B. Gibbs, D. Graham, and D.H. Tomlin: *Philos. Mag.*, 1963, vol. 8, pp. 1269–282.
27. ThermoCalc: The Precipitation Module (TC-PRISMA) User Guide 2020a. https://www.thermocalc.com/support/documentation/, Accessed June 30 2019.
28. H.I. Aaronson, M. Enomoto, and J.K. Lee: *Mechanisms of Diffusional Phase Transformations in Metals and Alloys*, CRC Press, Boca Raton, FL, 2016.
29. R. Wagner, R. Kampmann, and P.W. Voorhees: in: G. Kostorz, ed., *Phase Transformations in Materials*, Wiley-VCH Verlag GmbH, Weinheim, Germany, 2001, pp. 309–407.
30. R. Shi, N. Ma, and Y. Wang: *Acta Mater.*, 2012, vol. 60, pp. 4172–184.
31. G. Lindwall, U. Kattner, and C.E. Campbell: *Materials Data Curation System: Self diffusion and impurity diffusion*, NIST, Gaithersburg, 2017.
32. J.L. Murray: *Bull. Alloy Phase Diagrams*, 1981, vol. 2, pp. 320–34.
33. S. Kirklin, J.E. Saal, B. Meredig, A. Thompson, J.W. Doak, M. Aykol, S. Rühl, and C. Wolverton: *Comput. Mater.*, 2015, vol. 1, p. 15010.
34. J.E. Saal, S. Kirklin, M. Aykol, B. Meredig, and C. Wolverton: *JOM*, 2013, vol. 65, pp. 1501–509.
35. X.-G. Lu, M. Selleby, and B. Sundman: *CALPHAD*, 2005, vol. 29, pp. 68–89.
36. J. Ilavsky and P.R. Jemian: *J. Appl. Crystallogr.*, 2009, vol. 42, pp. 347–53.

Publisher's Note Springer Nature remains neutral with regard to jurisdictional claims in published maps and institutional affiliations.

Springer Nature or its licensor holds exclusive rights to this article under a publishing agreement with the author(s) or other rightsholder(s); author self-archiving of the accepted manuscript version of this article is solely governed by the terms of such publishing agreement and applicable law.